nanomaterials

MDPI

Article

Enhanced OER Performances of Au@$NiCo_2S_4$ Core-Shell Heterostructure

Yuepeng Lv †, Sibin Duan †, Yuchen Zhu, Peng Yin, and Rongming Wang *

Beijing Advanced Innovation Center for Materials Genome Engineering, Beijing Key Laboratory for Magneto-Photoelectrical Composite and Interface Science, School of Mathematics and Physics, University of Science and Technology Beijing, Beijing 100083, China; b20150331@xs.ustb.edu.cn (Y.L.); sibinduan@ustb.edu.cn (S.D.); cy931122@live.com (Y.Z.); yinpeng0537@163.com (P.Y.)

* Correspondence: rmwang@ustb.edu.cn

† These authors contributed equally to this work.

Received: 03 March 2020; Accepted: 23 March 2020; Published: 27 March 2020

Abstract: Transition metal sulfides have attracted a lot of attention as potential oxygen evolution reaction (OER) catalysts. Bimetallic sulfide possesses superior physicochemical properties due to the synergistic effect between bimetallic cations. By introducing a metal-semiconductor interface, the physicochemical properties of transition metal sulfide can be further improved. Using the solvothermal method, Au@$NiCo_2S_4$ core-shell heterostructure nanoparticles (NPs) and bare $NiCo_2S_4$ NPs were prepared. The measurement of the OER catalytic performance showed that the catalytic activity of Au@$NiCo_2S_4$ core-shell heterostructure was enhanced compared to bare $NiCo_2S_4$ NPs. At the current density of 10 mA cm^{-2}, the overpotential of Au@$NiCo_2S_4$ (299 mV) is lower than that of bare $NiCo_2S_4$ (312 mV). The Tafel slope of Au@$NiCo_2S_4$ (44.5 mV dec^{-1}) was reduced compared to that of bare $NiCo_2S_4$ (49.1 mV dec^{-1}), indicating its faster reaction kinetics. Detailed analysis of its electronic structure, chemical state, and electrochemical impedance indicates that the enhanced OER catalytic performances of bare Au@$NiCo_2S_4$ core-shell NPs were a result of its increased proportion of high-valance Ni/Co cations, and its increased electronic conductivity. This work provides a feasible method to improve OER catalytic performance by constructing a metal-semiconductor core-shell heterostructure.

Keywords: metal-semiconductor; core-shell; bimetallic sulfide; OER; structure-property relationship

1. Introduction

Due to the limited supply and the threat to the environment of fossil fuels, renewable and clean energies need to be developed. Hydrogen is an ideal energy substitute, with high energy density and zero carbon emission. Electrochemical water splitting is an environmentally friendly and promising method for hydrogen production [1,2]. However, the working potential of electrochemical water splitting is much higher than 1.23 V—the theoretical potential [3,4]. Reducing the overpotential and enhancing the stability of catalytic materials are the main research goals of electrochemical water splitting. OER as the anode of the electrochemical water splitting reaction is a multi-step reaction that requires high energy to form O–O^* bonds, leading to high overpotential and severely limiting hydrogen production efficiency [5]. Therefore, efficient catalysts are necessary to reduce the overpotential and enhance the OER reaction rate. IrO_2 and RuO_2 are recognized as the most effective OER catalysts, but the low supply and high price of these catalysts seriously limit their commercial applications [6–8].

Transition metals—with their nitrides, phosphides, oxides, hydroxides, sulfides, and selenides—are widely recognized as effective OER catalysts [4,9–14]. Transition metal sulfide is widely used in the field of OER catalysis due to its abundant supply, low price, superior catalytic activity, and stable performance. Co/Ni sulfides have been considered as potential catalysts for their multivalent properties and tunable electronical structure [15]. Compared with monometallic sulfides, bimetallic sulfides exhibit outstanding OER activities because they have more active sites, higher conductivity, larger electrochemical surface area, and higher structural stability [13,16–27]. Among the bimetallic catalysts, bimetallic nickel cobalt sulfides have become one of the most studied bimetallic structure compounds, due to their advantages of high conductivity and the redox reaction in which Ni and Co elements are more abundant in multi-valence than monometallic sulfides [22,28,29]. For example, (Ni, Co)S_2 nanosheet has a lower overpotential of 270 mV, compared to CoS_2 nanosheet (350 mV), and NiS_2 nanosheet (410 mV) at 10 mA cm^{-2}, which is due to its good mass/electron transfer properties, more catalytic active sites and facilitated adsorption to O^* [30].

To further enhance the OER catalytic properties and promote the application of bimetallic sulfides, designing heterostructures composed of bimetallic sulfide and metal is one of the most effective methods [31–35]. The enhanced physicochemical properties of metal-semiconductor heterostructures are mainly due to the interaction between metal and semiconductor [36,37]. Compared with yolk-shell and oligomer-like heterostructures, the core-shell heterostructure has the maximum contact interface, which can effectively enhance electron transmission along the interface, improve the electrical conductivity, and optimize the electronic structure [9,37,38]. For example, Au@NiS_x core-shell heterostructure has higher HER activity than Au-NiS_x yolk-shell and Au-NiS_x oligomer-like NPs. This is because the Au@NiS_x core-shell heterostructure has a larger contact interface, leading to promoted charge transfer and higher conductivity [39]. The OER activity of Au/$Ni_{12}P_5$ core-shell heterostructure has also been demonstrated to be improved by the electron interaction between Au and $Ni_{12}P_5$ [36].

Herein, Au@$NiCo_2S_4$ heterostructure and bare $NiCo_2S_4$ NPs were rationally designed and prepared through solvothermal methods. Using time-dependent experiments, the evolution mechanism of Au@$NiCo_2S_4$ NPs was studied. The measurements of the OER performance indicate that Au@$NiCo_2S_4$ core-shell heterostructure shows a high current density of 10 mA cm^{-2}, at a lower overpotential of 299 mV, and a lower Tafel slope of 44.5 mV dec^{-1}, compared with bare $CoNi_2S_4$ NPs.

2. Materials and Methods

2.1. Preparation of the Au@$NiCo_2S_4$ Core-Shell NPs

Au@$NiCo_2S_4$ core-shell heterostructure NPs were controllably synthesized using the seeded growth method. The synthesis method is shown in Figure 1. Typically, 0.05 g $Ni(acac)_2$ and 0.1 g $Co(acac)_2$ were dissolved in 16 mL oleylamine (OAm) in a three-necked flask. The solution was heated to 100 °C to form a clear solution. An amount of 3 ml toluene solution containing 0.03 g $HAuCl_4{\cdot}4H_2O$ was dropped into the solution afterwards. Au NPs were formed at 100 °C in the OAm by the reduction of the Au precursor, which were used as seeds during the subsequent growth of $NiCo_2S_4$ shells. The solution was kept at this temperature for 1 h and then heated to 210 °C. 0.123 g thiourea was added to the solution at 210 °C to serve as a sulfur source. The solution was then heated to 230 °C, and held at this temperature for 3 h. During this time, the $NiCo_2S_4$ shell formed and grew on the surface of the Au seeds. Finally, the solution was cooled to room temperature. The prepared sample was washed with a mixture of chloroform and acetone and collected by centrifugation. The solution was stirred during the whole reaction, and Ar gas was injected as the protective gas.

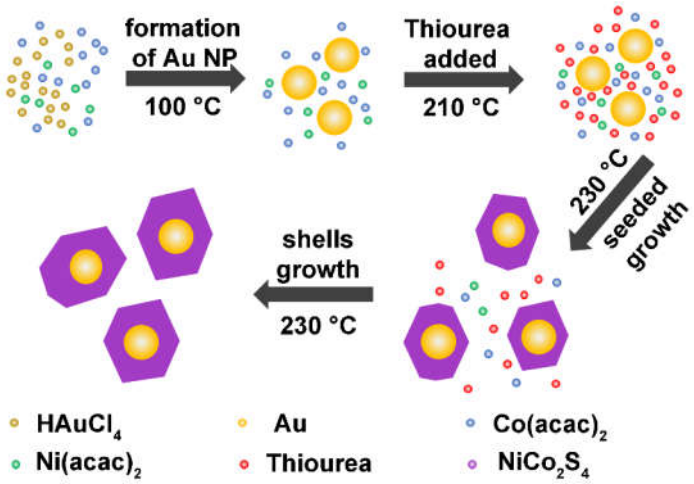

Figure 1. Diagram for the synthesis processes of Au@$NiCo_2S_4$ NPs. The core-shell structure was formed by the seeded growth of $NiCo_2S_4$ shells on Au NPs.

2.2. Preparation of the Bare $NiCo_2S_4$ NPs

The bare $NiCo_2S_4$ NPs were prepared by the typical solvothermal method. Amounts of 0.05 g $Ni(acac)_2$ and 0.1 g $Co(acac)_2$ were dissolved in 16 mL OAm in a three-necked flask. The solution was heated to 210 °C to form a clear solution. 0.123 g thiourea was added to the solution afterwards. The solution was then heated to 230 °C, and kept at this temperature for 3 h. After the solution was cooled to room temperature, the prepared sample was washed with a mixture of chloroform and acetone, and collected by centrifugation. The solution was stirred during the whole process, and Ar gas was injected as a protective gas.

2.3. Material Characterization

The crystal structures of the products were characterized by X-ray diffraction (XRD) using a Rigaku D/max 2200 PC diffractometer, with Cu Kα radiation (λ = 0.15406 nm). An Oxford X-Max80T energy dispersive X-ray spectrograph was used to measure the elemental composition and distribution of the products. A JEOL JEM-2200FS field emission transmission electron microscope (TEM, Tokyo, Japan, JEOL) was used to investigate the morphology of the samples. The atomic arrangements and microstructure of the as-grown samples were examined on a Titan ETEM G2 aberration-corrected transmission electron microscope (AC-TEM). A ULVAC-PHI Phi5000 VersaProbe III X-ray photoelectron spectrograph (XPS, Chigasaki, Japan, ULVAC-PHI) was used to measure the electronic structure and valence of the elements.

2.4. OER Catalytic Measurements

A CHI 760E electrochemical workstation was used to measure the OER catalytic performance of the as-prepared samples. The measurements were performed in a 1 M KOH solution, using a three-electrodes system. To prepare the working electrodes, a 5 mg sample was dispersed into 1 mL ethanol and stirred magnetically for 20 min. Then, 5 mg carbon black was added to the solution and stirred for 20 min. 100 μL 5 wt % Nafion was added to the solution, and the homogeneous ink was formed by stirred magnetically. 44 μL ink was dropped onto the surface of a piece of carbon paper (1 cm^2) and dried at room temperature to serve as the working electrode. About 0.2 mg of the sample was loaded onto the working electrode. The Hg/HgO and Pt plate were used as the reference electrode and counter electrode, respectively. Linear sweep voltammetry (LSV) was used to characterize OER catalytic performance, with a scan rate of 2 mV s^{-1}, and 95% iR compensation. The electrochemical impedance spectroscopy (EIS) of the samples was carried out by AC impedance, with a frequency range from 100,000 to 0.1 Hz. The stability of the samples was characterized by a current-time curve.

3. Results and Discussion

Core-shell NPs with a single crystal structure are difficult to be prepare because of the big differences in crystal structures and physicochemical properties between metal and sulfide [35]. Understanding the growth mechanism is helpful for their preparation and controlling their electrocatalytic performance. The time-dependent experiments were conducted in combination with with TEM and EDS analyses. Samples were collected from 0 to 180 min after thiourea was added. Figure S1a–f shows the morphologies of the collected samples. During the formation of Au@$NiCo_2S_4$ core-shell NPs, the Au NPs kept a five-fold symmetric morphology, and the size of Au NPs was also maintained at 8 ~ 10 nm. The shells gradually formed and thickened to about 10 nm. Table S1 shows the atomic ratios of Au to Co gradually decrease from 1 to 0.21. From 10 to 30 min, the atomic ratios of Co to S changed from 0.49 to 0.42. From 30 to 180 min, the atomic ratios of Co to S barely changed. This indicates that the sulfuration process has been completed at 30 min. The above process indicates that the evolution mechanism of Au@$NiCo_2S_4$ NPs is a typical seeded growth of $NiCo_2S_4$ shells on the Au NPs.

Figure 2 shows the XRD spectra of Au@$NiCo_2S_4$ and bare $NiCo_2S_4$ NPs, which confirms that the samples consist of cubic $NiCo_2S_4$ (JCPDS No. 43-1477) and cubic Au (JCPDS No. 99-0056). The impurity phase was not detected in the XRD patterns, indicating the high purity of the as-grown sample. Scherrer's equation ($d = 0.89\lambda/(\beta \cdot \cos\theta_B)$, where λ is the X-ray wavelength, θ_B is the Bragg diffraction angle and β is the full width at half maxima of the peak) was used to estimate the crystal sizes of the products. The crystal size of $NiCo_2S_4$ was calculated to be about 11.8 nm, using the peak of $NiCo_2S_4$ (311) at about 31.5°, and that of the peak of Au was calculated to be about 8.8 nm, using the peak of Au (111) at about 38.2°.

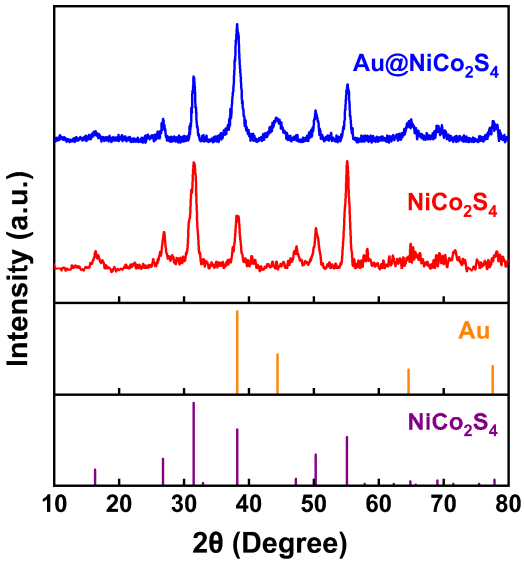

Figure 2. XRD patterns of as-prepared Au@$NiCo_2S_4$, and bare $NiCo_2S_4$ NPs.

The chemical composition of the synthesized samples was confirmed by the EDS measurements. The EDS spectra of Au@$NiCo_2S_4$ and bare $NiCo_2S_4$ NPs show that the products were composed of S, Co, Ni, and Au, as shown in Figure S2. The atomic ratio for S, Co, Ni, and Au for the Au@$NiCo_2S_4$ and bare $NiCo_2S_4$ NPs is also illustrated in Table S2. The TEM specimen holder may cause the additional signals of Si and Cu. The atomic percentages of Ni, Co, and S of the Au@$NiCo_2S_4$ heterostructure are 10.1%, 24.7%, and 59.9%, respectively. The atomic percentages of Ni, Co, and S of the bare $NiCo_2S_4$ NPs are 11.4%, 25.5%, and 63.1%, respectively. Compared with the stoichiometric proportion, the contents of S are slightly higher, possibly due to the adsorption of additional S on the surface of the NPs.

The morphologies and microstructures of the Au@$NiCo_2S_4$ and the bare $NiCo_2S_4$ NPs were characterized by TEM. As shown in Figure 3a, the interface between the darker Au cores and the lighter $NiCo_2S_4$ of the NPs is clean and smooth, without impurity phases, pores, layers or amorphous structure. The bonding between the Au cores and $NiCo_2S_4$ shells was good along the interface because no additional diffraction contrast from the strain was detected. The diameter of the cores is 8.2 ± 1.5 nm. The shell with lighter contrast has a polyhedral structure, with dimensions of 21.9 ± 5.5 nm. The morphologies of these NPs are mainly truncated octahedrons. In Figure S3a–e, the core-shell heterostructure was further confirmed by rotating the TEM samples. Regardless of the viewing angle, the Au NPs were always located at the center of the particles, indicating that the prepared sample was core-shell structure rather than Au NPs supported on the surface of $NiCo_2S_4$ NPs [39]. The atomic arrangements in the Au@$NiCo_2S_4$ NPs were investigated using AC-TEM. An Au@$NiCo_2S_4$ NP with a typical truncated octahedron morphology is shown in Figure 3b. At the atomic scale, no amorphous layer or impurity phase is observed, and the crystal lattice fringe of the $NiCo_2S_4$ shell layer is clear, indicating that Au@$NiCo_2S_4$ NPs crystallize well. The diameter of the Au core is ~ 9 nm, and the thickness of the $NiCo_2S_4$ shell is ~ 9 nm. The FFT pattern (Figure 3c) indicates that the shell of the NP is a cubic phase $NiCo_2S_4$ single crystal. The lattice spacing is 0.285 nm, corresponding to the $NiCo_2S_4$ (311) planes. To confirm the element distribution of Au@$NiCo_2S_4$ NPs, EDS mapping spectra were collected. The spectra shown in Figure S4 indicate that the Au element is only distributed in the core, while the other three elements are distributed in the shell. The polyhedron $NiCo_2S_4$ NPs are exhibited in Figure 3d for comparison. The size of bare $NiCo_2S_4$ NPs is 10.8 ± 2.1 nm. Figure 3e shows a typical $NiCo_2S_4$ polyhedron NP with almost perfect facets. The crystal lattice of the bare $NiCo_2S_4$ NP is clear. The FFT analysis (Figure 3f) demonstrates that the bare $NiCo_2S_4$ NP is a cubic phase $NiCo_2S_4$ single crystal. The lattice spacing was measured to be 0.331 nm, corresponding to the $NiCo_2S_4$ (220) plane. All the above results confirm that Au@$NiCo_2S_4$ NPs is core-shell structured, with single crystal shells.

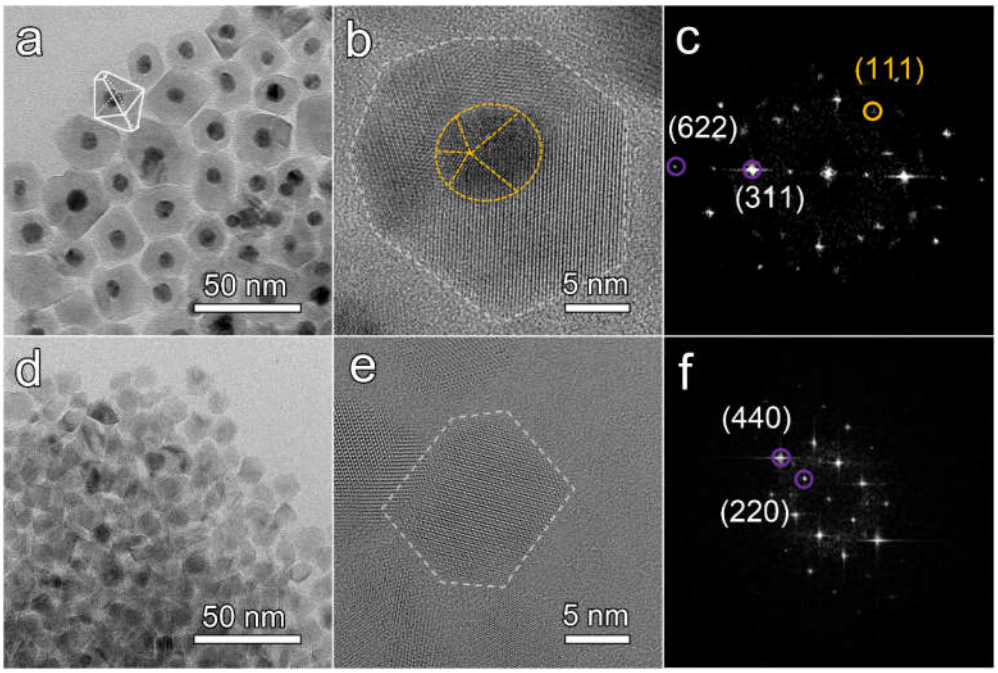

Figure 3. (**a**) Typical bright field TEM images of Au@$NiCo_2S_4$ NPs, (**b**) HRTEM images obtained by AC-TEM of an Au@$NiCo_2S_4$ NP, (**c**) FFT pattern of a Au@$NiCo_2S_4$ NP, (**d**) Typical bright field TEM images of $NiCo_2S_4$ NPs, (**e**) HRTEM images obtained by AC-TEM of a bare $NiCo_2S_4$ NP, (**f**) FFT pattern of a bare $NiCo_2S_4$ NP. In the FFT pattern, the diffraction spots of Au and $NiCo_2S_4$ are marked by yellow and purple circles, respectively.

The XPS spectra were used to characterize the chemical states and electronic structures of Au@$NiCo_2S_4$ and bare $NiCo_2S_4$ NPs. The full survey scan XPS spectra are shown in Figure S5. By

comparing the spectra, it can be confirmed that the full survey scan XPS spectrum of Au@$NiCo_2S_4$ is similar to that of bare $NiCo_2S_4$, except that the peak of Au 4f appears at 80–90 eV. Figure 4 and Figure S6 show high-resolution spectra of the Ni, Co, S, and Au of Au@$NiCo_2S_4$ and bare $NiCo_2S_4$ NPs, respectively. The Ni 2p high-resolution spectra are shown in Figure 4a. The fitting peaks positioned at 853.12–853.22 eV and 870.42–870.52 eV are assigned to Ni^{2+}, while the peaks at 854.92–855.04 eV and 872.22–872.34 eV correspond to Ni^{3+} [19]. The Co 2p high-resolution spectra are shown in Figure 4b. The fitting peaks positioned at 778.68–778.69 eV and 793.88–793.89 eV are assigned to Co^{3+}, while the peaks at 779.83–779.86 eV and 795.03–795.06 eV correspond to Co^{2+} [19]. Figure S5a shows the S 2p XPS spectra. The peaks positioned at 161.54–161.58 eV and 162.46–162.53 eV are assigned to S^{2-}, while the peaks at 162.94–163.00 eV and 163.84–163.97 eV are assigned to S^{-}. The peaks at 165.95–166.29 eV are assigned to SO_4^{2-}/SO_3^{2-}, which may be caused by oxidation of the surface sulfur [40]. The Au 4f XPS spectrum of the Au@$NiCo_2S_4$ is shown in Figure S5b.; the fitting peaks positioned at 84.16 eV and 87.81 eV are assigned to metallic Au, and the peaks at 85.19 eV and 88.74 eV can be assigned to Au^{+} [41]. These results indicate that Ni and Co atoms possess multi-valence in the bimetallic sulfides. The ratios of valence states are shown in Table S3. Compared with bare $NiCo_2S_4$, the ratio of Ni^{3+}:Ni^{2+} in Au@$NiCo_2S_4$ was increased, which is similar to the trend of Co^{3+}:Co^{2+}. These results indicate that there is strong electron interaction between Au and $NiCo_2S_4$. Due to the addition of Au NPs, the proportion of Co^{3+} and Ni^{3+} in $NiCo_2S_4$ NPs increases, which is beneficial to their electrochemical performances, because Ni^{3+}/Co^{3+} have been considered as active sites during the oxygen evolution [6].

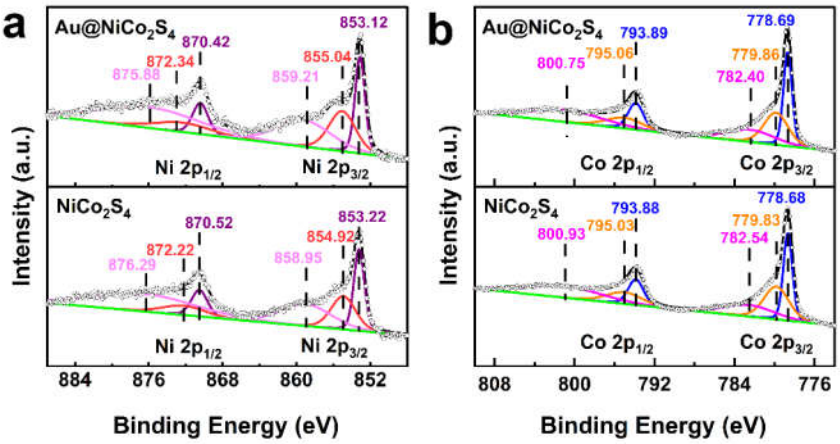

Figure 4. High resolution XPS spectra for the (**a**) Ni 2p, (**b**) Co 2p of Au@$NiCo_2S_4$, and $NiCo_2S_4$ NPs.

The OER catalytic performances of the Au@$NiCo_2S_4$ heterostructure and bare $NiCo_2S_4$ NPs were tested in alkaline solutions. The OER catalytic parameters are shown in Table S4. Figure 5a shows the polarization curves of the as-prepared samples. The overpotential of Au@$NiCo_2S_4$ NPs (299 mV) is lower than that of bare $NiCo_2S_4$ NPs (312 mV) at a current density of 10 mA cm^{-2}. The OER catalytic performance is improved by the interaction between Au NPs and $NiCo_2S_4$ shells. The overpotential of Au@$NiCo_2S_4$ NPs is comparable to the value of previously reported catalysts such as $NiCo_2S_4$@g-C_3N_4–CNT (320 mV, 10 mA·cm^{-2}) [19], $NiCo_2S_4$ nanoflakes (319 mV, 100 mA cm^{-2}) [16], and Au@$CoFeO_x$ (328 mV, 10 mA cm^{-2}) [9]. The Tafel slopes of Au@$NiCo_2S_4$ NPs and $NiCo_2S_4$ NPs are shown in Figure 5b. Compared with bare $NiCo_2S_4$ NPs (49.1 mV dec^{-1}), the Tafel slope of Au@$NiCo_2S_4$ (44.5 mV dec^{-1}) is lower, indicating that Au@$NiCo_2S_4$ NPs possess a superior reaction kinetic, and a faster mass/electron transport rate. The Tafel slopes of these two samples are comparable or superior to other OER catalysts such as $NiCo_2S_4$ nanoflakes (53.3 mV dec^{-1}) [16], $NiCo_2S_4$ (54.9 mV dec^{-1}) [6], Ni_3Se_2 (40.2 mV dec^{-1}) [13], $NiCo_2S_4$@NiFe LDH (46.3 mV dec^{-1}) [23] and P-Co-Ni-S nanosheets (61.1 mV dec^{-1}) [42]. All these results demonstrate that, due to the interaction between Au and $NiCo_2S_4$, Au@$NiCo_2S_4$ NPs exhibit better OER catalytic activity than bare $NiCo_2S_4$ NPs.

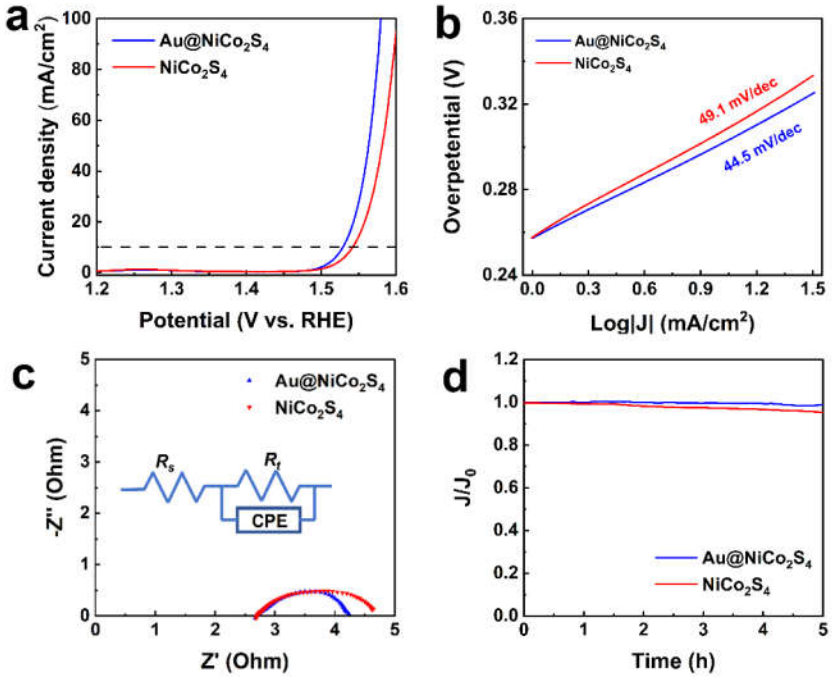

Figure 5. OER performances of Au@$NiCo_2S_4$, and bare $NiCo_2S_4$ NPs in 1 M KOH: (**a**) polarization curves (**b**) Tafel curves, (**c**) Nyquist plots, and (**d**) time–current curves.

To further analyze the electronical factors affecting the OER activity of the samples, the EIS of Au@$NiCo_2S_4$ and bare $NiCo_2S_4$ NPs were measured. The diameter of the Nyquist plots of Au@$NiCo_2S_4$ is smaller than that of bare $NiCo_2S_4$, as shown in Figure 5c. The equivalent circuit, fitted according to the EIS, is shown in the inset of Figure 5c. The charge transfer resistance R_t corresponds to the diameter of the Nyquist plot, and represents the resistance of mass transfer during the OER catalytic reaction, which is the decisive parameter affecting OER catalytic efficiency [43]. It can be seen that the R_t of Au@$NiCo_2S_4$ (1.6 Ω) is lower than that of bare $NiCo_2S_4$ (2.0 Ω). The decrease of R_t is due to the interaction between the Au NP and the $NiCo_2S_4$ shell, which can enhance the conductivity and shorten the length of charge diffusion [39]. The double-layer capacitance (C_d) of the NPs surface is reflected by the Y_0 value of the CPE, which represents the location of the absorbed molecules, and is related to the electrochemical surface area [36]. The Y_0 value of Au@$NiCo_2S_4$ NPs is much larger than that of bare $NiCo_2S_4$ NPs, as shown in Table S4, indicating that its effective surface area is larger than that of bare $NiCo_2S_4$ NPs, and that Au@$NiCo_2S_4$ core-shell NPs have more active sites and exhibit better OER activity. In addition, as demonstrated by the XPS results, in Au@$NiCo_2S_4$ NPs, the proportion of high-valance Ni and Co cations is increased. The high-valance Ni and Co cations are the active sites for OER, so the Au@$NiCo_2S_4$ core-shell NPs possess better OER catalytic activity than bare $NiCo_2S_4$ [6]. Therefore, benefiting from the lower R_t, larger effective surface area, the increased proportion of high-valence Ni and Co cations, and the single crystal $NiCo_2S_4$ shells, the Au@$NiCo_2S_4$ NPs possess better OER activity than bare $NiCo_2S_4$. As shown in Figure 5d, to test the stability of the materials, a current-time curve for the as-prepared NPs was characterized. Au@$NiCo_2S_4$ and bare $NiCo_2S_4$ have relatively excellent OER catalytic stability, maintaining 98.9%, and 95.2% after 5 hours, respectively. This indicates that Au@$NiCo_2S_4$ and bare $NiCo_2S_4$ NPs have a superior stability over a long period of OER catalysis. The stability of Au@$NiCo_2S_4$ core-shell NPs is superior to $NoCo_2S_4$ NPs, which should be attributed to the following factors: (1) The introduction of Au cores reduced the overpotential, thus reducing the driving force for the reconstruction of $NiCo_2S_4$ [9]. (2) The interface interaction between Au and $NiCo_2S_4$ increased the proportion of Co^{3+} and Ni^{3+}, thus enhancing the charge density at the specific domains and increasing the number of active sites [44]. (3) The larger effective surface area of Au@$NiCo_2S_4$ makes it easier for bubbles to detach from the electrode [45].

4. Conclusions

In summary, Au@$NiCo_2S_4$ and bare $NiCo_2S_4$ NPs were controllably prepared. The Au@$NiCo_2S_4$ sample exhibited a core-shell heterostructure with single crystal shells. The OER catalytic results confirm that the core-shell structure exhibits superior OER catalytic performance to bare $NiCo_2S_4$ NPs, which may be due to the interaction between Au and $NiCo_2S_4$. The XPS and EIS results demonstrated that the electronic conductivity, and the ratio of high-valance Ni and Co, were improved with the Au-$NiCo_2S_4$ interaction, which are beneficial to its electrocatalytic performance. The overpotential and Tafel slope of the Au@$NiCo_2S_4$ heterostructure NPs is 299 mV at 10 mA cm^{-2} and 44.5 mV dec^{-1}, respectively. The construction of metal-semiconductor core-shell heterostructure will provide more chances for its application in the field of electrochemical water splitting.

Supplementary Materials: Figure S1. TEM images of Au@$NiCo_2S_4$ NPs evolution experiment. Table S1. The ratios of elements at different times of Au@$NiCo_2S_4$ NPs evolution experiment. Figure S2. EDS spectra of the Au@$NiCo_2S_4$ and bare $NiCo_2S_4$ NPs. Table S2. Atomic ratio of Au, Ni, Co and S of Au@$NiCo_2S_4$ and bare $NiCo_2S_4$ NPs calculated by EDS. Figure S3. Angle-dependent TEM characterization of Au@$NiCo_2S_4$ NPs verifying the core-shell of the products. The shells produced in the outer shell of the NP were reasoned from the carbon deposit induced by the long-time high-energy electron irradiation. Scale bar 20 nm. Figure S4. HAADF-STEM images and STEM-EDS mappings for the elements Au, Ni, Co, and S of Au@$NiCo_2S_4$ NPs. Figure S5. XPS survey spectra of Au@$NiCo_2S_4$ and bare $NiCo_2S_4$ NPs. Figure S6. High resolution XPS spectra for the (a) S 2p, (b) Au 4f of Au@$NiCo_2S_4$ and bare $NiCo_2S_4$ NPs. Table S3. XPS peaks area ratio of Ni, and Co of Au@$NiCo_2S_4$ and bare $NiCo_2S_4$ NPs. Table S4. Electrochemical and equivalent circuit simulation parameters of the samples including Au@$NiCo_2S_4$, and bare $NiCo_2S_4$ NPs.

Author Contributions: Y.L, S.D. and R.W. conceived and designed the experiments. Y.L. and P.Y. synthesized the samples. Y.L. performed the OER catalytic experiments. Y.Z. performed the TEM characterization. Y.L, S.D. and R.W. wrote and refined the manuscript. All authors analyzed the data, discussed the results, and approved the manuscript. Y. L. and S.D. contributed equally to this work. All authors have read and agreed to the published version of the manuscript.

Funding: This research was funded by the National Key Research and Development Program of China (No. 2018YFA0703700), the National Natural Science Foundation of China (Nos. 51971025 and 51901012), the Fundamental Research Funds for the Central Universities (FRF-TP-17-073A1) and 111 Project (No. B170003).

Conflicts of Interest: The authors declare no conflict of interest。

References

1. Guo, Y.N.; Park, T.; Yi, J.W.; Henzie, J.; Kim, J.; Wang, Z.L.; Jiang, B.; Bando, Y.; Sugahara, Y.; Tang, J.; et al. Nanoarchitectonics for transition-metal-sulfide-based electrocatalysts for water splitting. *Adv. Mater.* **2019**, *31*, 34, doi:10.1002/adma.201807134.
2. You, B.; Sun, Y.J. Innovative strategies for electrocatalytic water splitting. *Acc. Chem. Res.* **2018**, *51*, 1571–1580, doi:10.1021/acs.accounts.8b00002.
3. Du, X.C.; Huang, J.W.; Zhang, J.J.; Yan, Y.C.; Wu, C.Y.; Hu, Y.; Yan, C.Y.; Lei, T.Y.; Chen, W.; Fan, C.; et al. Modulating electronic structures of inorganic nanomaterials for efficient electrocatalytic water splitting. *Angew. Chem. Int. Ed.* **2019**, *58*, 4484–4502, doi:10.1002/anie.201810104.
4. Wang, Y.Y.; Yan, D.F.; El Hankari, S.; Zou, Y.Q.; Wang, S.Y. Recent progress on layered double hydroxides and their derivatives for electrocatalytic water splitting. *Adv. Sci.* **2018**, *5*, 32, doi:10.1002/advs.201800064.
5. Zhang, B.; Zheng, X.L.; Voznyy, O.; Comin, R.; Bajdich, M.; Garcia-Melchor, M.; Han, L.L.; Xu, J.X.; Liu, M.; Zheng, L.R.; et al. Homogeneously dispersed multimetal oxygen-evolving catalysts. *Science* **2016**, *352*, 333–337, doi:10.1126/science.aaf1525.
6. Kang, Z.; Guo, H.J.; Wu, J.; Sun, X.; Zhang, Z.; Liao, Q.L.; Zhang, S.C.; Si, H.N.; Wu, P.W.; Wang, L.; et al. Engineering an earth-abundant element-based bifunctional electrocatalyst for highly efficient and durable overall water splitting. *Adv. Funct. Mater.* **2019**, *29*, 1, doi:10.1002/adfm.201807031.
7. McCrory, C.C.L.; Jung, S.; Ferrer, I.M.; Chatman, S.M.; Peters, J.C.; Jaramillo, T.F. Benchmarking hydrogen evolving reaction and oxygen evolving reaction electrocatalysts for solar water splitting devices. *J. Am. Chem. Soc.* **2015**, *137*, 4347–4357, doi:10.1021/ja510442p.
8. Xu, Y.; Tu, W.; Zhang, B.; Yin, S.; Huang, Y.; Kraft, M.; Xu, R. Nickel nanoparticles encapsulated in few-layer nitrogen-doped graphene derived from metal-organic frameworks as efficient bifunctional electrocatalysts for overall water splitting. *Adv. Mater.* **2017**, *29*, 1605957, doi:10.1002/adma.201605957.

9. Strickler, A.L.; Escudero-Escribano, M.; Jaramillo, T.F. Core-shell Au@metal-oxide nanoparticle electrocatalysts for enhanced oxygen evolution. *Nano Lett.* **2017**, *17*, 6040–6046, doi:10.1021/acs.nanolett.7b02357.
10. Wang, Y.; Chen, L.; Yu, X.; Wang, Y.; Zheng, G. Superb alkaline hydrogen evolution and simultaneous electricity generation by Pt-decorated Ni_3N nanosheets. *Adv. Energy Mater.* **2017**, *7*, 1601390, doi:10.1002/aenm.201601390.
11. Wang, F.; Li, Y.; Shifa, T.A.; Liu, K.; Wang, F.; Wang, Z.; Xu, P.; Wang, Q.; He, J. Selenium-enriched nickel selenide nanosheets as a robust electrocatalyst for hydrogen generation. *Angew. Chem. Int. Ed.* **2016**, *55*, 6919–6924, doi:10.1002/anie.201602802.
12. Chen, P.Z.; Zhou, T.P.; Zhang, M.X.; Tong, Y.; Zhong, C.G.; Zhang, N.; Zhang, L.D.; Wu, C.Z.; Xie, Y. 3D nitrogen-anion-decorated nickel sulfides for highly efficient overall water splitting. *Adv. Mater.* **2017**, *29*, 6, doi:10.1002/adma.201701584.
13. Sivanantham, A.; Shanmugam, S. Nickel selenide supported on nickel foam as an efficient and durable non-precious electrocatalyst for the alkaline water electrolysis. *Angew. Chem. Int. Ed.* **2017**, *203*, 485–493, doi:10.1016/j.apcatb.2016.10.050.
14. Guan, C.; Xiao, W.; Wu, H.J.; Liu, X.M.; Zang, W.J.; Zhang, H.; Ding, J.; Feng, Y.P.; Pennycook, S.J.; Wang, J. Hollow Mo-doped CoP nanoarrays for efficient overall water splitting. *Nano Energy* **2018**, *48*, 73–80, doi:10.1016/j.nanoen.2018.03.034.
15. Kulkarni, P.; Nataraj, S.K.; Balakrishna, R.G.; Nagaraju, D.H.; Reddy, M.V. Nanostructured binary and ternary metal sulfides: Synthesis methods and their application in energy conversion and storage devices. *J. Mater. Chem. A* **2017**, *5*, 22040–22094, doi:10.1039/c7ta07329a.
16. Yu, J.; Lv, C.X.; Zhao, L.; Zhang, L.X.; Wang, Z.H.; Liu, Q.Y. Reverse microemulsion-assisted synthesis of $NiCo_2S_4$ nanoflakes supported on nickel foam for electrochemical overall water splitting. *Adv. Mater. Interfaces* **2018**, *5*, 8, doi:10.1002/admi.201701396.
17. Liu, Q.; Jin, J.; Zhang, J. $NiCo_2S_4$@graphene as a bifunctional electrocatalyst for oxygen reduction and evolution reactions. *ACS Appl. Mater. Inter.* **2013**, *5*, 5002–5008, doi:10.1021/am4007897.
18. Liu, D.; Lu, Q.; Luo, Y.; Sun, X.; Asiri, A.M. $NiCo_2S_4$ nanowires array as an efficient bifunctional electrocatalyst for full water splitting with superior activity. *Nanoscale* **2015**, *7*, 15122–15126, doi:10.1039/c5nr04064g.
19. Han, X.; Zhang, W.; Ma, X.; Zhong, C.; Zhao, N.; Hu, W.; Deng, Y. Identifying the activation of bimetallic sites in $NiCo_2S_4$@g-C_3N_4-CNT hybrid electrocatalysts for synergistic oxygen reduction and evolution. *Adv. Mater.* **2019**, *31*, e1808281, doi:10.1002/adma.201808281.
20. Zhu, W.X.; Ren, M.R.; Hu, N.; Zhang, W.T.; Luo, Z.T.; Wang, R.; Wang, J.; Huang, L.J.; Suo, Y.R.; Wang, J.L. Traditional $NiCo_2S_4$ phase with porous nanosheets array topology on carbon cloth: A flexible, versatile and fabulous electrocatalyst for overall water and urea electrolysis. *ACS Sustain. Chem. Eng.* **2018**, *6*, 5011–5020, doi:10.1021/acssuschemeng.7b04663.
21. Gong, Y.Q.; Wang, J.L.; Lin, Y.; Yang, Z.; Pan, H.L.; Xu, Z.F. Synthesis of 1D to 3D nanostructured $NiCo_2S_4$ on nickel foam and their application in oxygen evolution reaction. *Appl. Surf. Sci.* **2019**, *476*, 600–607, doi:10.1016/j.apsusc.2019.01.100.
22. Sivanantham, A.; Ganesan, P.; Shanmugam, S. Hierarchical $NiCo_2S_4$ nanowire arrays supported on ni foam: An efficient and durable bifunctional electrocatalyst for oxygen and hydrogen evolution reactions. *Adv. Funct. Mater.* **2016**, *26*, 4661–4672, doi:10.1002/adfm.201600566.
23. Liu, J.; Wang, J.; Zhang, B.; Ruan, Y.; Lv, L.; Ji, X.; Xu, K.; Miao, L.; Jiang, J. Hierarchical $NiCo_2S_4$@NiFe LDH heterostructures supported on nickel foam for enhanced overall-water-splitting activity. *ACS Appl. Mater. Inter.* **2017**, *9*, 15364–15372, doi:10.1021/acsami.7b00019.
24. Li, X.X.; Wang, X.T.; Xiao, K.; Ouyang, T.; Li, N.; Liu, Z.Q. In situ formation of consubstantial $NiCo_2S_4$ nanorod arrays toward self-standing electrode for high activity supercapacitors and overall water splitting. *J. Power Sources* **2018**, *402*, 116–123, doi:10.1016/j.jpowsour.2018.09.021.
25. Gao, Q.Y.; Wang, X.Q.; Shi, Z.Y.; Ye, Z.R.; Wang, W.C.; Zhang, N.; Hong, Z.L.; Zhi, M.J. Synthesis of porous $NiCo_2S_4$ aerogel for supercapacitor electrode and oxygen evolution reaction electrocatalyst. *Chem. Eng. J.* **2018**, *331*, 185–193, doi:10.1016/j.cej.2017.08.067.
26. Li, J.W.; Zhuang, Q.N.; Xu, P.M.; Zhang, D.W.; Wei, L.C.; Yuan, D.S. Three-dimensional lily-like CoNi2S4 as an advanced bifunctional electrocatalyst for hydrogen and oxygen evolution reaction. *Chin. J. Catal.* **2018**, *39*, 1403–1410, doi:10.1016/S1872-2067(18)63053-0.
27. Huang, R.; Chen, W.; Zhang, Y.; Huang, Z.; Dai, H.; Zhou, Y.; Wu, Y.; Lv, X. Well-designed cobalt-nickel sulfide microspheres with unique peapod-like structure for overall water splitting. *J. Colloid Interface Sci.* **2019**, *556*, 401–410, doi:10.1016/j.jcis.2019.08.093.

28. Xiao, J.; Wan, L.; Yang, S.; Xiao, F.; Wang, S. Design hierarchical electrodes with highly conductive $NiCo_2S_4$ nanotube arrays grown on carbon fiber paper for high-performance pseudocapacitors. *Nano Lett.* **2014**, *14*, 831–838, doi:10.1021/nl404199v.
29. Xu, M.J.; Xu, R.J.; Zhao, Y.; Chen, L.B.; Huang, B.Y.; Wei, W.F. Hierarchically porous Ni monolith@branch-structured NiCo2O4 for high energy density supercapacitors. *Prog. Nat. Sci.* **2016**, *26*, 276–282, doi:10.1016/j.pnsc.2016.05.012.
30. Zhang, J.; Bai, X.; Wang, T.; Xiao, W.; Xi, P.; Wang, J.; Gao, D.; Wang, J. Bimetallic Nickel Cobalt Sulfide as Efficient Electrocatalyst for Zn-Air Battery and Water Splitting. *Nano Micro Lett.* **2019**, *11*, 2, doi:10.1007/s40820-018-0232-2.
31. Liu, X.; Iocozzia, J.; Wang, Y.; Cui, X.; Chen, Y.; Zhao, S.; Li, Z.; Lin, Z. Noble metal–metal oxide nanohybrids with tailored nanostructures for efficient solar energy conversion, photocatalysis and environmental remediation. *Energ. Environ. Sci.* **2017**, *10*, 402–434, doi:10.1039/c6ee02265k.
32. Wang, M.; Ye, M.; Iocozzia, J.; Lin, C.; Lin, Z. Plasmon-mediated solar energy conversion via photocatalysis in noble metal/semiconductor composites. *Adv. Sci.* **2016**, *3*, 1600024, doi:10.1002/advs.201600024.
33. Feng, J.; Liu, J.; Cheng, X.; Liu, J.; Xu, M.; Zhang, J. Hydrothermal cation exchange enabled gradual evolution of Au@ZnS-AgAuS yolk-shell nanocrystals and their visible light photocatalytic applications. *Adv. Sci.* **2018**, *5*, 1700376, doi:10.1002/advs.201700376.
34. Sun, Y.H.; Yang, X.Z.; Zhao, H.F.; Wang, R.M. Non-symmetric hybrids of noble metal-semiconductor: Interplay of nanoparticles and nanostructures in formation dynamics and plasmonic applications. *Prog. Nat. Sci.* **2017**, *27*, 157–168, doi:10.1016/j.pnsc.2017.03.006.
35. Lv, Y.; Duan, S.; Wang, R. Structure design, controllable synthesis, and application of metal-semiconductor heterostructure nanoparticles. *Prog. Nat. Sci.* **2020**, *30*, 1–12, doi:10.1016/j.pnsc.2019.12.005.
36. Xu, Y.Y.; Duan, S.B.; Li, H.Y.; Yang, M.; Wang, S.J.; Wang, X.; Wang, R.M. $Au/Ni_{12}P_5$ core/shell single-crystal nanoparticles as oxygen evolution reaction catalyst. *Nano Res.* **2017**, *10*, 3103–3112, doi:10.1007/s12274-017-1527-1.
37. Duan, S.B.; Wang, R.M. $Au/Ni_{12}P_5$ core/shell nanocrystals from bimetallic heterostructures: In situ synthesis, evolution and supercapacitor properties. *NPG Asia Mater.* **2014**, *6*, e122, doi:10.1038/am.2014.65.
38. Wang, R. The dynamic of the peel. *Nat. Catal.* **2020**, doi:10.1038/s41929-020-0451-z.
39. Lv, Y.; Duan, S.; Zhu, Y.; Guo, H.; Wang, R. Interface control and catalytic performances of Au-NiS heterostructures. *Chem. Eng. J.* **2020**, *382*, 122794, doi:10.1016/j.cej.2019.122794.
40. Feng, J.X.; Wu, J.Q.; Tong, Y.X.; Li, G.R. Efficient hydrogen evolution on Cu nanodots-decorated Ni_3S_2 nanotubes by optimizing atomic hydrogen adsorption and desorption. *J. Am. Chem. Soc.* **2018**, *140*, 610–617, doi:10.1021/jacs.7b08521.
41. Moon, S.Y.; Song, H.C.; Gwag, E.H.; Nedrygailov, I.I.; Lee, C.; Kim, J.J.; Doh, W.H.; Park, J.Y. Plasmonic hot carrier-driven oxygen evolution reaction on Au nanoparticles/TiO_2 nanotube arrays. *Nanoscale* **2018**, *10*, 22180–22188, doi:10.1039/c8nr05144e.
42. Zhang, F.; Ge, Y.; Chu, H.; Dong, P.; Baines, R.; Pei, Y.; Ye, M.; Shen, J. Dual-functional starfish-like P-doped Co-Ni-S nanosheets supported on nickel foams with enhanced electrochemical performance and excellent stability for overall water splitting. *ACS Appl. Mater. Inter.* **2018**, *10*, 7087–7095, doi:10.1021/acsami.7b18403.
43. Hu, J.M.; Zhang, J.Q.; Cao, C.N. Oxygen evolution reaction on IrO_2-based DSA (R) type electrodes: Kinetics analysis of Tafel lines and EIS. *Int. J. Hydrogen Energy* **2004**, *29*, 791–797, doi:10.1016/j.ijhydene.2003.09.007.
44. Guo, Y.N.; Tang, J.; Wang, Z.L.; Kang, Y.M.; Bando, Y.; Yamauchi, Y. Elaborately assembled core-shell structured metal sulfides as a bifunctional catalyst for highly efficient electrochemical overall water splitting. *Nano Energy* **2018**, *47*, 494–502, doi:10.1016/j.nanoen.2018.03.012.
45. Li, M.; Wang, H.; Zhu, Y.; Tian, D.; Wang, C.; Lu, X. Mo/Mo2C encapsulated in nitrogen-doped carbon nanofibers as efficiently integrated heterojunction electrocatalysts for hydrogen evolution reaction in wide pH range. *Appl. Surf. Sci.* **2019**, *496*, 143672, doi:10.1016/j.apsusc.2019.143672.

.